

**ADVANCED TECHNIQUES IN UV MICROSCOPY:
INTEGRATING DEEP LEARNING FOR AUTOFOCUSING,
WHOLE SLIDE IMAGING OPTIMIZATION, AND SPICULE
DETECTION IN BONE MARROW ASPIRATIONS**

A Dissertation
Presented to
The Academic Faculty

by

Ajay Rajaraman Subramanian

In Partial Fulfillment
of the Requirements for the Degree
Master of Science in the
Georgia Institute of Technology

Georgia Institute of Technology
May 2024

COPYRIGHT © 2024 BY AJAY RAJARAMAN SUBRAMANIAN

**ADVANCED TECHNIQUES IN UV MICROSCOPY: INTEGRATING
DEEP LEARNING FOR AUTOFOCUSING, WHOLE SLIDE
IMAGING OPTIMIZATION, AND SPICULE DETECTION IN BONE
Marrow Aspirations**

Approved by:

Dr. Francisco E. Robles, Advisor
Wallace H. Coulter Department of Biomedical
Engineering
Georgia Institute of Technology

Dr. Shu Jia
Wallace H. Coulter Department of Biomedical
Engineering
Georgia Institute of Technology

Dr. Ahmet F Coskun
Wallace H. Coulter Department of Biomedical
Engineering
Georgia Institute of Technology

Date Approved: [April 26, 2024]

ACKNOWLEDGEMENTS

I would like to express my sincere gratitude to the following individuals and organizations who have contributed to the completion of this thesis:

Dr. Francisco Robles: I am deeply thankful to Dr. Francisco Robles for his invaluable guidance, unwavering support, and insightful feedback throughout every stage of this research project. His expertise and encouragement have been instrumental in shaping my academic journey.

Committee Members: I extend my heartfelt appreciation to my committee members, Dr. Shu Jia and Dr. Ahmet F Coskun, for their insightful feedback, guidance, and expertise in evaluating this thesis. Their contributions have enriched the quality of my work and guided me towards its completion.

Peers and Colleagues: I would like to thank my fellow colleagues, Vishy Gorti, Nischita Kaza, Srinidhi Bharadwaj, Zhenmin Li, Zhe Guang, Case Edmondson, Robby Nelson, Paloma Casteleiro Costa, and Caroline Filan, for their camaraderie, encouragement, and valuable discussions throughout this journey.

Family and Friends: To my family and friends, whose unwavering support, understanding, and encouragement sustained me during the challenges of this research endeavor, I am deeply grateful.

Institutional Support: I acknowledge the Wallace H. Coulter Department of Biomedical Engineering for providing access to resources, facilities, and research opportunities that facilitated the completion of this thesis.

I am grateful to all those mentioned above and anyone else who has supported me along this academic journey, directly or indirectly. Your contributions have been invaluable and deeply appreciated.

I would also like to acknowledge Generative AI tools such as ChatGPT and Microsoft Copilot for assisting me in refining scientific language and rephrasing certain sentences to enhance the clarity and coherence of this thesis.

TABLE OF CONTENTS

ACKNOWLEDGEMENTS	iii
LIST OF FIGURES	vii
LIST OF SYMBOLS AND ABBREVIATIONS	ix
SUMMARY	x
CHAPTER 1. INTRODUCTION	1
1.1 Specific Aims	4
CHAPTER 2. Single-Shot Autofocusing	5
2.1 Introduction	5
2.2 Methods and Results	6
2.2.1 Experimental Setup	6
2.2.2 Data Collection and Image processing	7
2.2.3 Rayleigh Range calculation	10
2.2.4 Deep Learning model	11
2.2.5 Model Prediction Workflow	15
2.2.6 MATLAB Graphical User Interface	15
2.3 Discussion and Future work	17
CHAPTER 3. Whole slide imaging	18
3.1 Introduction	18
3.2 Methods and Results	18
3.2.1 Components in the Compact UV-System	19
3.2.2 Motor Optimization in the X, Y, Z direction	20
3.2.3 Data Collection	21
3.2.4 Graphical User Interface	25
3.3 Discussion and Future Work	26
CHAPTER 4. Deep-ultraviolet microscopy for analysis of bone marrow aspirate adequacy	28
4.1 Introduction	28
4.2 Methods and Results	29
4.2.1 Portable, LED-based UV system	29
4.2.2 Clinical Study	31
4.2.3 Statistical Analysis	32
4.2.4 Deep Learning for Automated Spicule Detection	32
4.2.5 Whole slide scanning via automated UV microscopy	36
4.3 Discussion and Future Work	38
CHAPTER 5. Conclusion	40
REFERENCES	42

LIST OF TABLES

Table 1 Comparison between True labels and Predicted labels by the autofocusing algorithm developed using the Compact UV microscopy.	13
Table 2 Comparison between True labels and Predicted labels by the autofocusing algorithm developed using the Compact UV microscopy.	14
Table 3 Results from the clinical study for bedside naked eye inspection (A) and visual UV inspection (B) of unstained bone marrow aspirate smears compared to ground truth histopathologist examination of stained slides. [referred from [44]].....	31
Table 4 Results from the clinical study for bedside naked eye inspection (A) and visual UV inspection (B) of unstained bone marrow aspirate smears compared to ground truth histopathologist examination of stained slides.[Referred from [44]]	35

LIST OF FIGURES

Figure 1 (a) Measured molar extinction coefficient spectra for tested materials. (b) Measured B spectra for tested materials [referred from [9]]	2
Figure 2 Schematic of the deep-UV microscope consisting of an ultrabroadband plasma source, short-pass dichroic mirror, UV band-pass filters, UV microscope objective, and UV-sensitive camera. [referred from [16]]	6
Figure 3 Compact UV microscope schematic [referred from [31]].....	7
Figure 4 Stack of Data from -15 microns to +15 microns.	8
Figure 5– A) Blood Cells B) Brain Tissue C) Frozen Section and D) Prostate Tissue	8
Figure 6 Bone Marrow Aspiration A) Spiculate Region and B) Aspiculated Region.....	9
Figure 7 – A) Pre-processed image of Prostate Tissue B) Corresponding image split into multiple patches.	10
Figure 8 –Image for Rayleigh Length (Range).....	11
Figure 9 Modified MobileNetV2 to do regression instead of Classification[referred from [33]].....	12
Figure 10 A) region in a sample with dirt, B) region in a sample with spicule	15
Figure 11 Deep Learning model workflow.....	16
Figure 12 MATLAB Graphical User Interface.....	16
Figure 13 A) MT1 Thorlabs stage used for Z-stage operation B) XRN25 XY Thorlabs stage used for XY stage Operation.	20
Figure 14 Stage translation in the X or Y direction between one field of view to another generates an overlap of 10%.	21
Figure 15 Manual inspection of the smear under the microscope to determine the four different points of the smear.	22
Figure 16 Stage translation in the X or Y direction moving in a S shaped pattern.	23
Figure 17 Stitched whole slide image using ImageJ software.....	24
Figure 18 Graphical user interface Layout.	25
Figure 19 UV microscopy system for the assessment of bone marrow aspirate quality. [referred from [43]].....	29
Figure 20 Wide-field unfixed and unstained pseudocolored UV image of a spiculated bone marrow aspirate (A) and the corresponding white-light bright-field microscopy image after fixing and staining (B). The red arrowheads point to spicules present in the smear [referenced from [16]].	30
Figure 21 Automated spicule detection algorithm including UV image preprocessing and object detection steps[referred from [44]].	34
Figure 22 Sample network output images from images with (left) and without (right) spicules.[referred from [44]].....	35
Figure 23 (A) Pseudo-colored UV whole slide scan of an unstained, spiculated bone marrow aspirate smear (top) and a brightfield whole slide scan of the same stained smear (bottom) captured at low (left) and high (middle, right) magnifications. (B) Corresponding whole slide scans for an aspicular bone marrow aspirate smear. Low and high magnification whole slide scans are composed of 225 images in a 15x15 grid with approximately 8%. overlap. Yellow arrows indicate megakaryocytes present in the bone	

marrow aspirate. Scale bars: 3mm (left), 300 μ m (middle), and 40 μ m (right).[referred
from [44]]..... 37

LIST OF SYMBOLS AND ABBREVIATIONS

GANS	Generative Adversarial Networks
TIF	Tag Image File Format
CNN	Convolutional Neural Network
Z_R	Rayleigh Range
GPU	Graphics Processing Unit
GUI	Graphical User Interface
LED	Light-emitting diode
Microns	Micrometer
λ	Wavelength
ω_0	Beam Waist
RPI4	Raspberry Pi 4

SUMMARY

Deep-ultraviolet (UV) microscopy enables label-free, high-resolution, quantitative molecular imaging and enables unique applications in biomedicine. This is achieved by leveraging the unique absorption of different biomolecules in the deep UV spectrum (200~400nm). While UV microscopy has historically been limited by phototoxicity concerns, recent advances in UV imaging hardware have allowed for live cell imaging for more than six hours with no observable photodamage.

This proposal aims to expand the capabilities of UV microscopy for biomedical applications using CNN based architectures. Initially, we will employ a custom benchtop multispectral microscope for single-shot autofocus. Subsequently, we will utilize a low-cost compact UV microscope for automated whole-slide imaging, incorporating single-shot autofocus as well. Additionally, the compact UV microscope will be employed for automated spicule detection in bone marrow aspirations to enable an untrained clinician to use the device.

CHAPTER 1. INTRODUCTION

Optical microscopy has a rich history in examining the structure and function of biological samples. Over time, various microscopy techniques have emerged, each with distinct characteristics. These differences encompass how they produce contrast in images, their capability to observe live cells, their resolution, and their imaging speed.

Brightfield microscopy stands out as one of the most widely used methods for imaging biological samples. However, its primary limitation lies in its inability to provide sufficient contrast for crucial biomolecules like nucleic acids, proteins, and lipids within the visible light spectrum. To enhance contrast for these biomolecules, staining is necessary. Yet, this process typically involves fixing cells or tissues, precluding the study of live cells. Fluorescence microscopy has emerged as a prevalent and potent method for investigating cells, wherein specific molecules are labeled with fluorophores. These fluorescent tags are excited by particular light wavelengths, emitting visible light that can be captured to produce high-resolution images with targeted molecular contrast. While this technique has facilitated substantial biological breakthroughs, it does come with several inherent drawbacks. Firstly, preparing samples with fluorescent labels can be laborious, costly, and reliant on chemical reagents that might not be readily accessible. Moreover, fluorescence microscopy is prone to photobleaching, which reduces the technique's ability to perform longitudinal imaging and interferes with biomolecular quantification. Additionally, fluorophores can impede the study of biological processes[1].

To mitigate these challenges, numerous label-free techniques have been developed, leveraging the inherent optical properties of biological samples. Examples include Raman microscopy[2-3], autofluorescence imaging[4], dark-field microscopy[5],[6], and quantitative phase imaging (QPI)[7], [8]. While these methods offer alternative means of

generating contrast without disturbing samples, they still entail significant trade-offs in terms of system complexity, cost, speed, and information provided, thereby constraining their versatility.

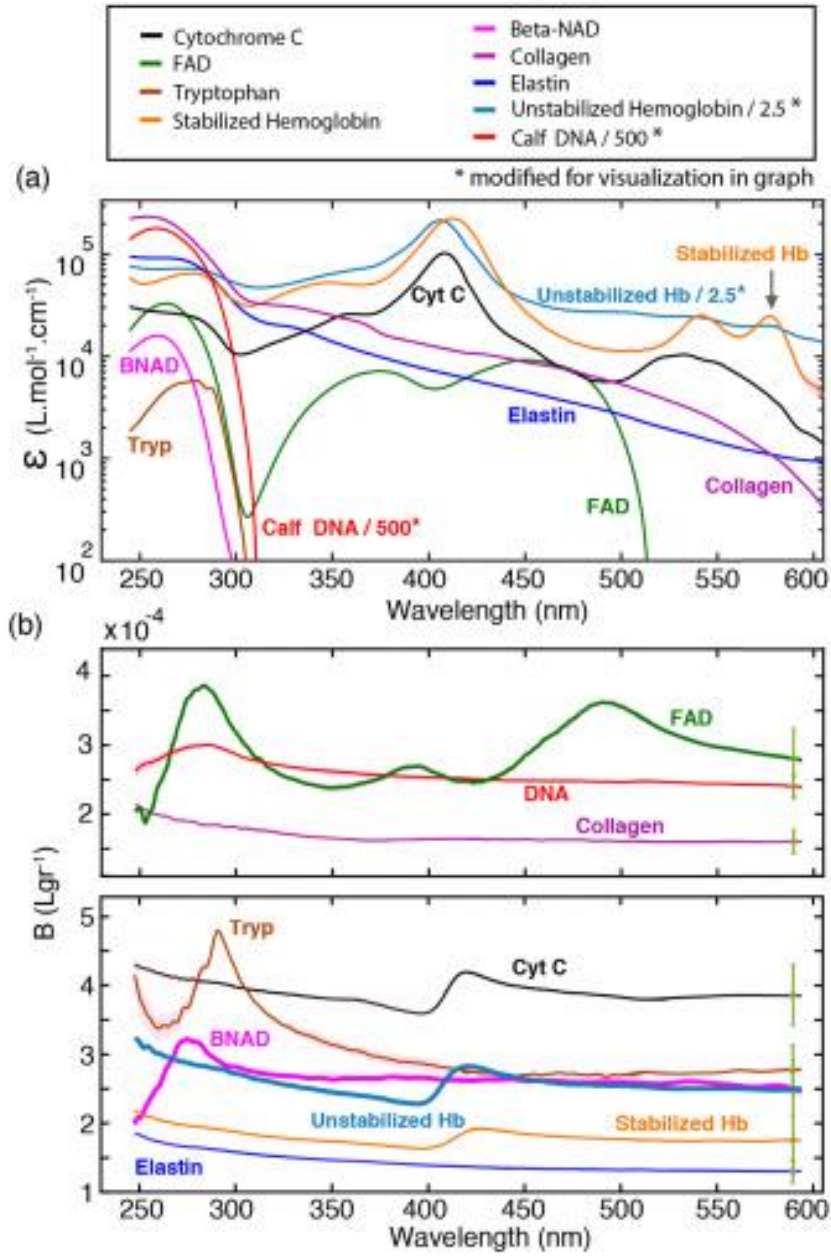


Figure 1 (a) Measured molar extinction coefficient spectra for tested materials. (b) Measured B spectra for tested materials [referred from [9]]

UV microscopy has been historically overlooked due to phototoxicity concerns, but hardware advancements and proper management of UV exposure have enabled contiguous live cell imaging for several hours[10], [11]. Deep-ultraviolet (UV) microscopy enables label-free, high-resolution, quantitative molecular imaging by leveraging unique absorption properties of biomolecules, such as nucleic acids, in the UV region of the spectrum (200-400nm) as depicted in Figure 1[9]. In the past two decades, deep-UV microscopy has been demonstrated for quantitative live-cell mass mapping, hematology analysis, and prostate cancer tissue characterization including the development of corresponding neural networks[12], [13], [14], [15], [16], [17], [18], [19], [20], [21].

Microscopic slides in pathology present several challenges, including time-consuming manual examination, variability in interpretation among pathologists, and the potential for human error. Convolutional neural networks (CNNs) offer promising solutions to these issues by automating the analysis of microscopic images[22]. By training on large datasets of annotated slides, CNNs can learn to identify and classify cellular structures, tissue patterns, and pathological features with high accuracy. This automated analysis not only speeds up the diagnostic process but also reduces the reliance on subjective human judgment, leading to more consistent and reliable results[23]. Moreover, CNNs can assist pathologists in detecting subtle abnormalities or rare patterns that may be overlooked during manual examination, thereby improving diagnostic accuracy and patient outcomes. Additionally, CNNs can facilitate the integration of quantitative metrics into pathology practice, enabling more objective assessments of disease severity and treatment response[24]. Overall, CNNs hold great promise for transforming the field of pathology by augmenting the capabilities of pathologists, enhancing diagnostic accuracy, and ultimately improving patient care.

1.1 Specific Aims

In this work, we seek to expand the capability of UV microscopy by using an already developed simple, low-cost systems and custom benchtop multispectral microscope that are well-suited for point-of-care applications and applying existing systems to further our understanding of use of the application of Artificial Intelligence in these systems. The overall aims of this project are as follows:

- 1) Implement Single-Shot Autofocusing in UV microscopy.
- 2) Develop an algorithm for automating Spicule Detection
- 3) Implement a strategy to capture whole slide imaging of a sample using Deep UV Microscopy.

These aims collectively aim to enhance the efficiency, accuracy, and applicability of UV microscopy techniques, paving the way for broader utilization in various fields, including healthcare and research.

CHAPTER 2. SINGLE-SHOT AUTOFOCUSING

2.1 Introduction

Ensuring proper focus when examining samples under a microscope is critical for two primary reasons. Firstly, specimens often exhibit varying topography, and secondly, live cells may cause the sample to drift out of focus due to movement[25]. Manual focusing over a large field of view can be challenging and is not always the preferred method. While some solutions involve costly hardware setups or require powerful GPUs for deploying deep learning models like GANs[26], which can map out-of-focus features to appear focused, or require multiple images to determine the best focus[27], there is an alternative approach

In this study, a single shot autofocusing algorithm is employed. This algorithm predicts a value that indicates the distance between the field of view and the optimal focus plane. By utilizing predictive algorithms, it estimates the distance and automatically adjusts the focus position in a single step. By analyzing image features and patterns, the algorithm determines the optimal focus position without the need for manual adjustments. The approach taken is a modification to what is presented in [25], here they use GANs to predict the autofocusing output, whereas the strategy adopted for this study will be a CNN based architecture where the value predicted indicates how far the sample is from the actual focus. The reason for choosing CNN over GANs is because the computational power required for GANs is much larger than that of CNN[28], [29], [30]. This automation streamlines the focusing process, reducing both time and effort required for imaging. As a result, it presents a practical solution for high-throughput microscopy applications.

2.2 Methods and Results

This section begins by providing an overview of the microscopes utilized, highlighting their significance. It then smoothly transitions into the process of data collection and the subsequent training of the deep learning model. Lastly, it concludes by detailing the implementation of the trained model within a MATLAB Graphical User Interface (GUI).

2.2.1 Experimental Setup

2.2.1.1 Custom Benchtop Multispectral Microscope

The custom benchtop multispectral microscope operates as a UV microscope designed for rapid imaging of live, unstained cells at various discrete UV wavelengths. Illustrated in Figure 2, the system utilizes a broad-band, laser-driven plasma source alongside a series of band-pass filters to adjust the imaging wavelength. This adjustment is made to align with the absorption peaks of key biochemical components within human cells [16]. This system has 220/239/255/280/300/415nm bandpass filters. The camera present in this system is a UV sensitive camera. The sample can be translated and adjusted for focusing via a three-axis high-precision motorized stage (MLS2031; Thorlabs).

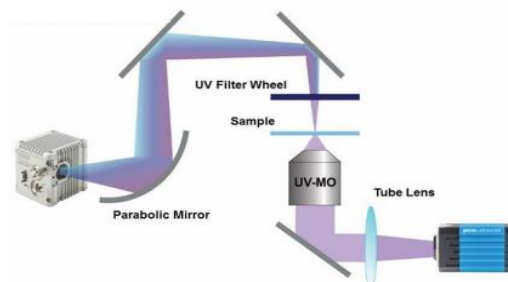


Figure 2 Schematic of the deep-UV microscope consisting of an ultrabroadband plasma source, short-pass dichroic mirror, UV band-pass filters, UV microscope objective, and UV-sensitive camera. [referred from[16]]

2.2.1.2 Compact UV System

As illustrated in Figure 3, the compact UV system shares similarities with the Custom Benchtop multispectral microscope but operates on a single wavelength, specifically 255 nm. This system is notably more cost-effective due to its utilization of surface mount LED technology for sample illumination, in contrast to the laser-driven plasma light source used in the Custom Benchtop multispectral microscope. Additionally, the narrow band LED illumination at 255 nm obviates the necessity for a UV bandpass filter unless you are imaging glass slides. The selection of the 255 nm wavelength is based on the significant absorption of nucleic acids within this spectral range, resulting in heightened intracellular nuclear contrast[31].

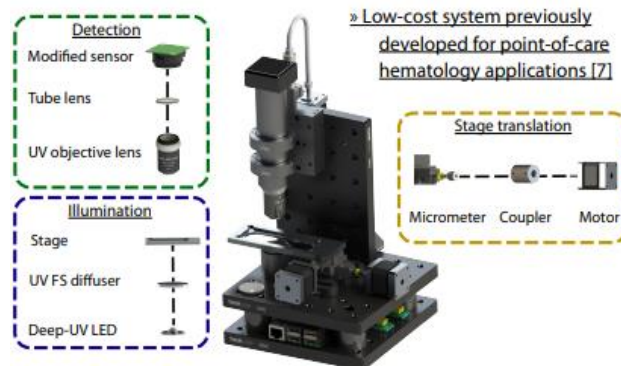


Figure 3 Compact UV microscope schematic [referred from [31]]

2.2.2 Data Collection and Image processing

Following a visual inspection to assess the variation in smear thickness, data collection was conducted accordingly. The examination revealed thickness variations ranging from approximately -9 microns to +9 microns within a sample. Consequently, multiple data stacks were gathered spanning from -15 microns to +15 microns with a step size of 0.5

microns, as illustrated in Figure 4. The data collection process involved samples obtained from diverse tissues and cells, including Blood smears, Frozen Sections of brain, and formalin fixed paraffin embedded (FFPE) tissues of Brain and prostate tissue sections, utilizing the Custom Benchtop multispectral microscope at 255 nm wavelength, as depicted in Figure 5. The LMU-20X-UVB objective was used for capturing the images with a 20x magnification. The working distance of this objective is 4.1 mm.

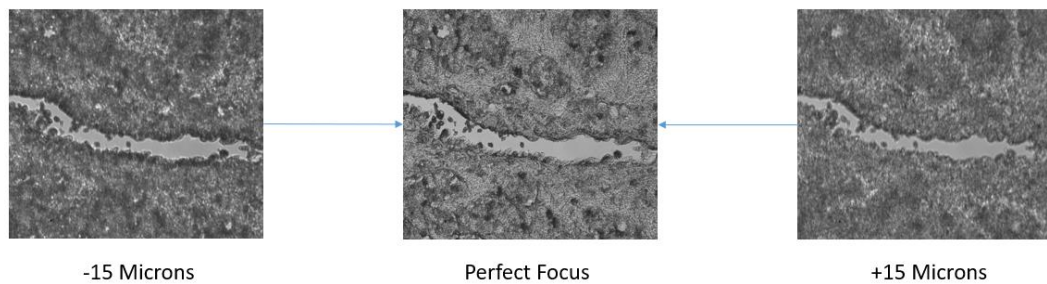


Figure 4 Stack of Data from -15 microns to +15 microns.

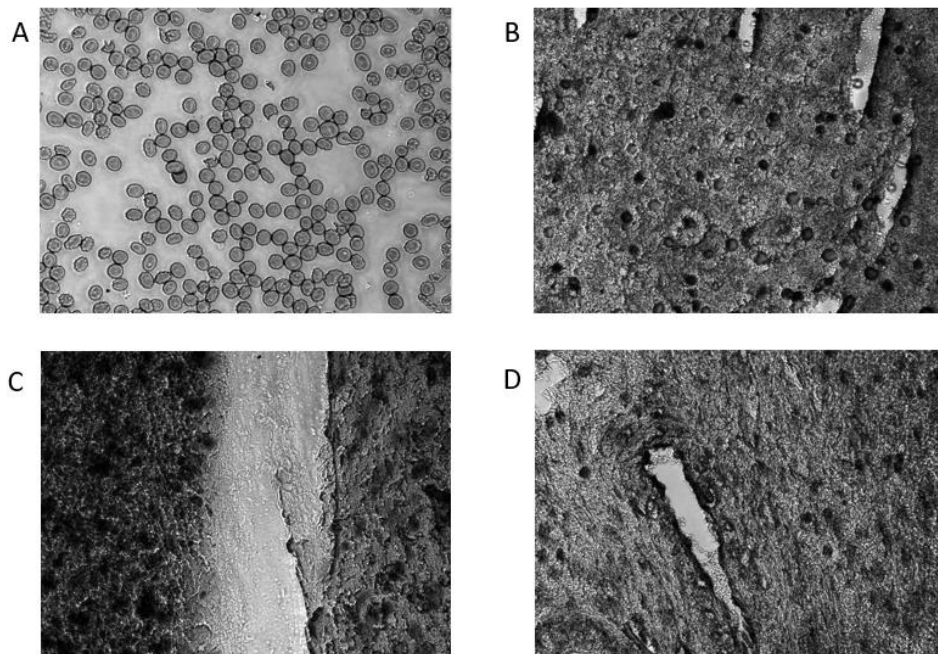


Figure 5– A) Blood Cells B) Brain Tissue C) Frozen Section and D) Prostate Tissue

Bone marrow aspiration images from -23.7 microns to +23.7 microns with a step size of 1.58 microns was captured using the Custom UV microscope as depicted in Figure 6. The LMU-5X-UVB objective was used for capturing the images with a 5x magnification. The working distance of this objective is 37.3 mm.

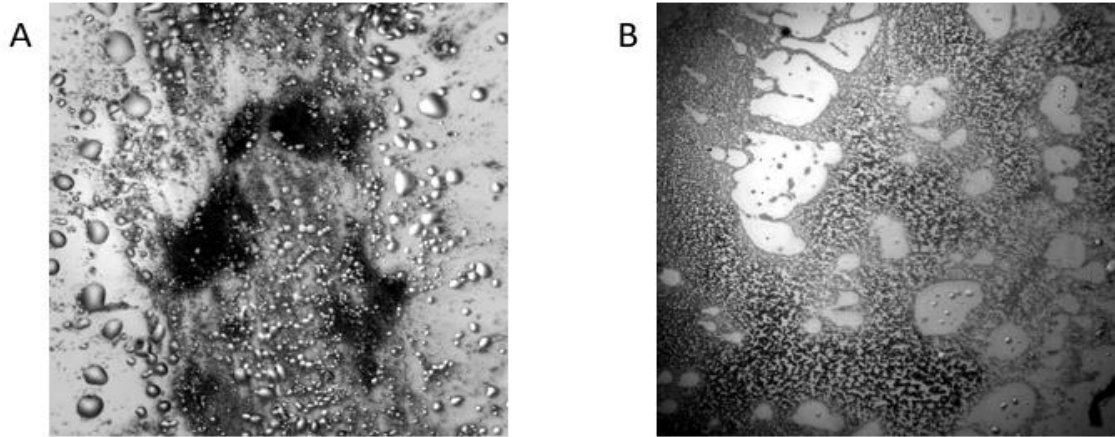


Figure 6 Bone Marrow Aspiration A) Spiculate Region and B) Asplicated Region

The captured images were saved in TIF format to ensure no data compression occurred. Each sample was accompanied by a corresponding background image capture. This background image serves the purpose of normalizing the images. Following normalization, a 99th percentile correction was applied, removing 1% outliers from the data.

Subsequently, the images underwent preprocessing to convert them into multiple patches, serving as input for the deep learning model. The images converted into multiple patches are illustrated in Figure 7.

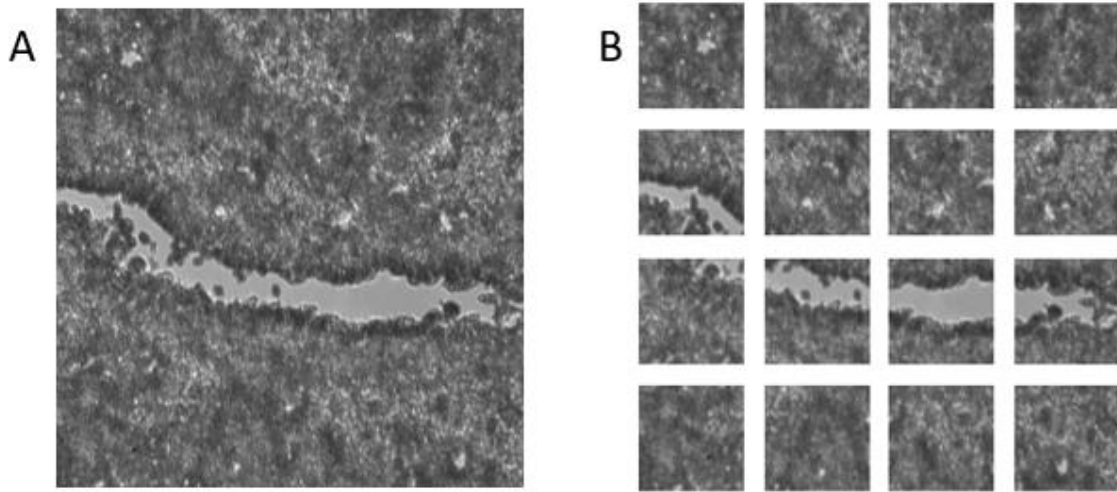


Figure 7 – A) Pre-processed image of Prostate Tissue B) Corresponding image split into multiple patches.

2.2.3 Rayleigh Range calculation

The Rayleigh Range is a term used in optics which helps to compute the distance along the propagation direction of a focused beam where the beam radius increases by a factor of $\sqrt{2}$ from its minimum value at the focus as depicted in Figure 8. In terms of focusing an image, being within the Rayleigh range ensures that the focused spot is relatively small and well-defined. This means that objects at different distances from the focal point will still be in relatively sharp focus. However, beyond the Rayleigh range, the focused spot starts to spread out, and objects at different distances from the focal point may not be as sharply focused.

$$Z_R = \frac{\pi\omega_0^2}{\lambda}$$

ω_0 is the beam waist radius at the focus, and λ is the wavelength of the light.

$$\omega_0 = \frac{\lambda}{\pi * N.A} \text{ (approximately)}$$

Where N.A is the numerical Aperture

For the LMU-5X-UVB N.A is 0.12. Therefore, the ω_0 value is 676.408 nm. This gives a value of 5.636 microns for Z_R .

For the LMU-20X-UVB N.A is 0.39. Therefore, the ω_0 value is 208.1 nm. This gives a value of 0.5336 microns for Z_R .

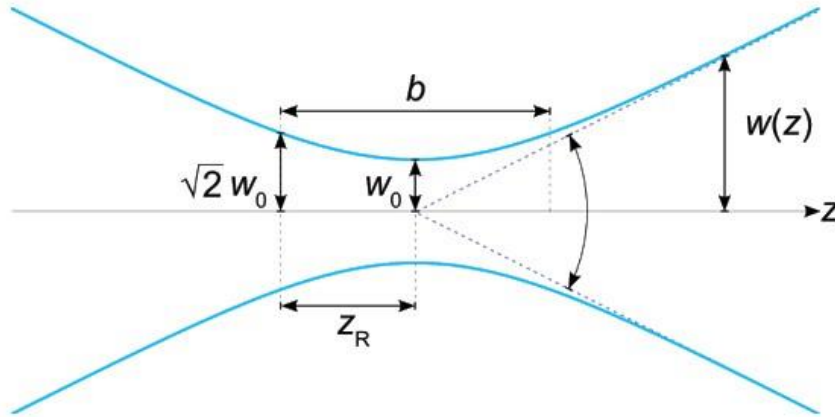


Figure 8 –Image for Rayleigh Length (Range)

2.2.4 Deep Learning model

MobilenetV2 is a lightweight convolutional neural network (CNN) architecture specifically designed for mobile and embedded vision applications[32]. The architecture of MobileNetV2 consists of a series of convolutional layers, followed by depth wise separable convolutions, inverted residuals, bottleneck design, linear bottlenecks, and squeeze-and-excitation (SE) blocks. The mobilenetV2 last layers were modified so that instead of returning a classification output, the network was modified to give a regression

output as depicted in figure 9. Two separate deep learning models using the same architecture were deployed one for the Custom Benchtop microscope and the second for the Compact UV system. For both the models the Adam Optimizer was used, and the Huber loss was used for training the model. These networks were trained in Python 3.9 with TensorFlow 2 on a NVIDIA GeForce RTX 2080Ti GPU for 100 epochs with a batch size of 8.

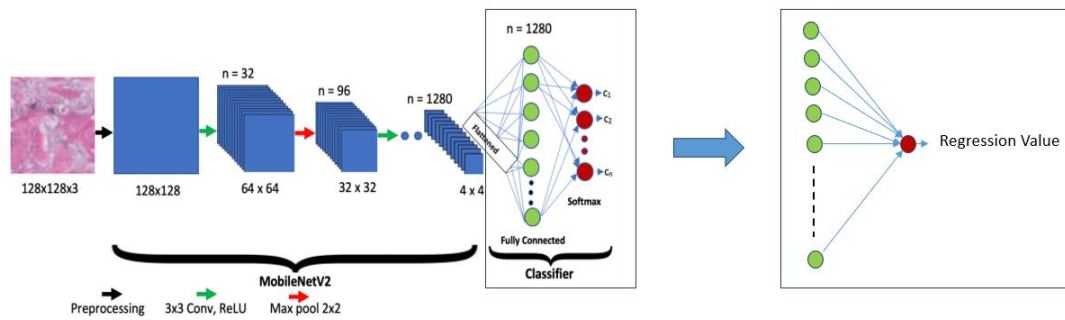


Figure 9 Modified MobileNetV2 to do regression instead of Classification[referred from [33]].

2.2.4.1 Custom Benchtop Microscope

The study gathered images from various cell and tissue types, including blood smears, frozen sections, and FFPE tissue sections, using a Custom Benchtop multispectral microscope. Thirty samples were examined, with each sample yielding approximately 4-5 sets of data stacks. Each data stack comprised 61 images, ranging from -15 microns to +15 microns with a step size of 0.5 microns. These images were then subdivided into multiple patches measuring 4 by 4 pixels each. In total, there were approximately 30 samples * 4 sets * 61 images * 16 patches, resulting in a substantial dataset for analysis.

For data analysis purposes, an 80-20 split was implemented, allocating 80% of the dataset for training the model, and reserving the remaining 20% for testing its performance. The model has a mean square error of 0.1437. Given that the Rayleigh range for the 20x objective was 0.588, the predictions generated by the model always stayed within this range. Table 1 shows the comparison between True label and the predicted label for a few regions.

Table 1 Comparison between True labels and Predicted labels by the autofocus algorithm developed using the Compact UV microscopy.

True Label	Predicted Label
1.5 microns	1.94 microns
-6 microns	- 6.24 microns
10 microns	10.46 microns
11.5 microns	11.04 microns
-14.5 microns	14.29 microns

2.2.4.2 Compact UV microscope

Collected bone marrow aspiration images comprised two distinct types: spiculated regions and asplicated regions. Seven spiculated samples and seven asplicated samples were utilized in the study. From each sample, four sets of data stacks were collected. Within each region, 31 images were captured, ranging from -23.7 microns to +23.7 microns with a step size of 1.58 microns. Thus, the total dataset comprised 14 samples * 4 regions * 31

images. Two additional samples were collected for testing purpose. The model has a Mean Squared Error of 14.669. Despite the model having a MSE of 14.669 the output predicted by the network is still in focus because the Rayleigh range is 5.636 microns, and the confocal parameter is 11.6 microns. The predictions from the model always ended up being in this range. Table 2 shows the comparison between the true label and the predicted label for a few regions.

Table 2 Comparison between True labels and Predicted labels by the autofocus algorithm developed using the Compact UV microscopy.

True Label	Predicted Output
23.7 microns	20.54 microns
-14.22 microns	-9.48 microns
4.74 microns	3.024 microns
-31.6 microns	-28.44 microns
-7.9 microns	-2.6 microns

It can be observed that for a few regions the difference between the true label and the predicted label is slightly higher because that region might be a spiculated region or might have a RBC cluster. There are regions which might have dirt as well. This might also affect the predictions. Figure 10A shows a dirt region used for the prediction and Figure 10 B shows the spicule region used for the prediction.

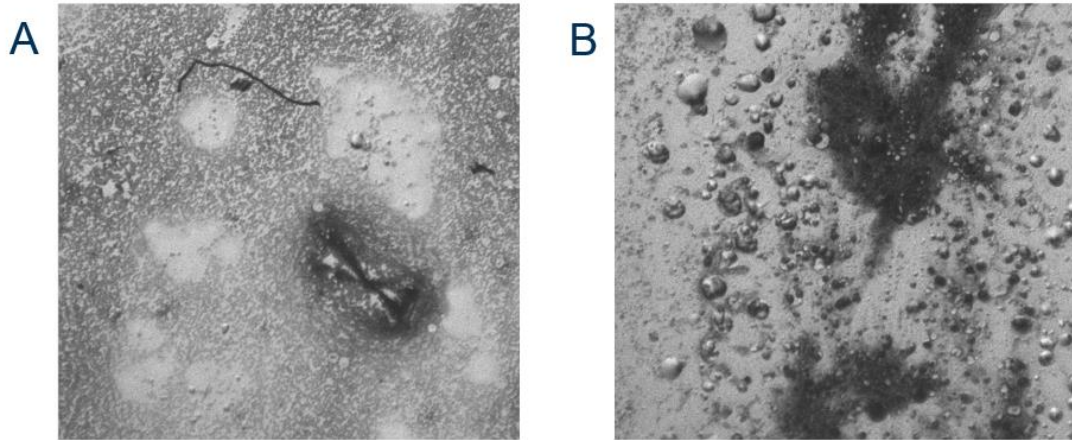


Figure 10 A) region in a sample with dirt, B) region in a sample with spicule

2.2.5 Model Prediction Workflow

The initial step involves preprocessing the image, which includes normalization and applying 99th percentile correction. Following this, the image is partitioned into patches, with each patch serving as input for the deep learning model. Once the model makes predictions for each patch, a hard vote is conducted on all the predictions. The predicted value with the highest number of votes is then considered as the final prediction. This process is depicted in Figure 11.

2.2.6 MATLAB Graphical User Interface

The MATLAB GUI was crafted utilizing the MATLAB App Designer tool by my colleague, Robby Nelson. Notably, the GUI initially lacked an integrated autofocus button. The design of this button, including its structure and size, was realized using MATLAB. However, the unique functionality of the autofocus button was achieved by integrating Python on the backend. The MATLAB GUI layout is showcased in Figure 12.

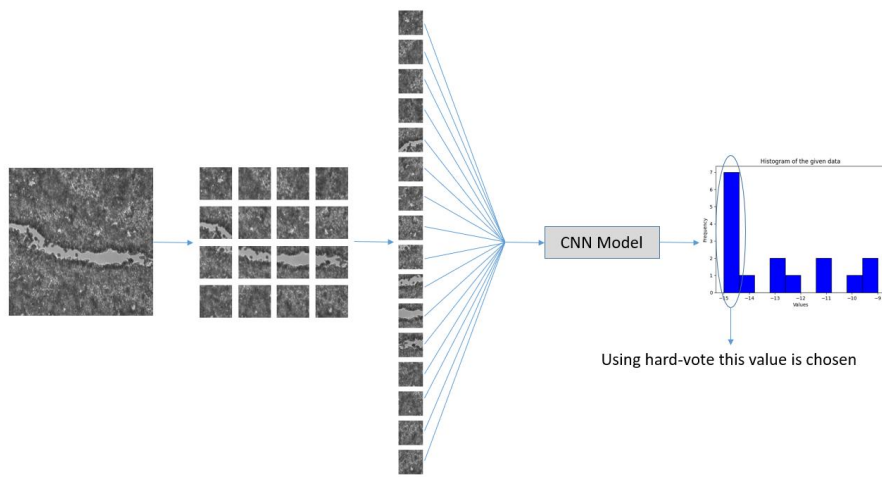


Figure 11 Deep Learning model workflow.



Figure 12 MATLAB Graphical User Interface

2.3 Discussion and Future work

In this chapter, we delved into the process of data collection and the implementation of the autofocusing algorithm on both the Custom Benchtop multispectral microscope and the compact UV system. For each system, two models were deployed, both achieving a MSE of 0.588 and 14.669 respectively. Despite having these MSE values the output generated by the model is always right because of the Rayleigh range of 0.58 microns for the Custom Benchtop multispectral microscope (owing to the use of the LMU-20X-UVB objective) and a Rayleigh range of 5.636 microns for the compact UV system (attributed to the utilization of the LMU-5X-UVB objective).

Furthermore, we described the pipeline for the deep learning model, demonstrating its integration within the MATLAB GUI. Currently, efforts are underway to enhance the compact system by incorporating larger sample stages, augmenting illumination power at the sample, and integrating variable magnifications. These modifications aim to transform the compact system into a more versatile label-free molecular imager.

CHAPTER 3. WHOLE SLIDE IMAGING

3.1 Introduction

Whole slide imaging is crucial in medicine because it allows entire slides to be digitized at high resolution. This means users can zoom in and examine cellular structures in detail, which can lead to more accurate diagnoses. Digital slides are also easier to store, organize, and retrieve compared to traditional slides. This simplifies the maintenance of comprehensive archives of patient samples, which is useful for retrospective studies, research, and quality assurance efforts.

Current methods for whole slide imaging typically involve expensive hardware setups[34] or may encounter difficulties in maintaining focus and uniformity throughout the entire slide, especially when dealing with uneven sample thickness or variations in staining intensity[35]. Also, the scanning times of whole slide imaging can be quite time consuming. In this chapter, a whole slide imaging technique is implemented on the Compact UV system using affordable stepper motors and a readily available microcontroller, the Raspberry Pi 4B. The goal is to reduce the scanning time as little as possible.

3.2 Methods and Results

This section begins by providing an overview of the components in the compact UV system. It then transitions into the process of motor optimization and data collection. Lastly, it concludes by integrating the Autofocusing algorithm deployed with the Compact UV system and deploying a GUI in python for operating this system freely.

3.2.1 Components in the Compact UV-System

In Chapter 2, we discussed how the components of the Compact UV system were carefully chosen to make it adaptable for Point-of-Care (POC) settings. Precision in the stage of this UV microscope was crucial to scan a target sample region accurately, without overlap or within a known range of overlap, to ensure precise analysis. To achieve this accuracy in stage control at a low cost, we opted for a configuration using stepper motors and micrometres. By combining high-resolution motors with low gear-ratio micrometres, we were able to achieve sub-micron step sizes in all three axes (X, Y, and Z) at a total cost of approximately \$1,000.

For the X and Y axes, micrometres are connected to their respective motors through custom machined adapters. These adapters are designed with bores that match the diameters of the micrometres and motor spindles, along with set screw taps for secure fastening. The Z-axis micrometre is connected to its motor through a driveshaft. Our Compact UV microscope utilizes 1.8° step angle bipolar stepper motors for the X and Y axes (XRN25 XY, Thorlabs) and a 0.9° step angle bipolar stepper motor for the Z-axis translator (MT1, Thorlabs). These stages are illustrated in Figure 13. The scan range in all three axes is 0.5 inches and can be extended by selecting appropriate stages[31].



Figure 13 A) MT1 Thorlabs stage used for Z-stage operation B) XRN25 XY Thorlabs stage used for XY stage Operation.

3.2.2 Motor Optimization in the X, Y, Z direction

As mentioned earlier, the high-resolution stepper motor has a step angle of 0.9° , and the MT1 micrometre travels 635 micrometres for every revolution. With a motor step size of 1, the translation is approximately 1.58 micrometres. Micro stepping can be employed with this motor, offering finer control with a $\frac{1}{4}$ step size translating to 0.396 micrometres or a $\frac{1}{2}$ step size resulting in 0.793 micrometres. Micro stepping is particularly beneficial when using the LMU-20X-UVB objective. However, for the LMU-5X-UVB, micro stepping is unnecessary due to the Rayleigh range being around 5.8 micrometres, eliminating the need for such a small step size. On the other hand, the low-resolution stepper motor has a step angle of 1.8° , and the XRN25 XY micrometre travels 500 micrometres for every revolution. With a motor step size of 1, the translation is approximately 2.5 micrometres. While using the LMU-5X-UVB objective it can be observed that by setting the step size to 500, the translation increases to 1250 micrometres. Choosing a step size of 500 ensures a 10% overlap between adjacent fields of view, as illustrated in Figure 14. Maintaining a minimum 10% overlap between field of views is essential when stitching images to create a whole slide image while using the 5X objective. While working with the LMU-20X-

UVB objective the step size of 100 generated an overlap of 16% between two adjacent field of views.



Figure 14 Stage translation in the X or Y direction between one field of view to another generates an overlap of 10%.

3.2.3 Data Collection

3.2.3.1 Determining the overall step size in the X and Y direction

To determine the number of images needed for whole slide stitching, it's essential to calculate the overall step size in both the X and Y directions. Since each sample may vary in size, accurately determining this step size is crucial for capturing complete slide images. Determining the step size is crucial even on the objective that is being used. As mentioned earlier, the translation between one field of view and another with a 10% overlap is 1250 micrometers or 500 steps for the 5X objective. The user, imaging the sample, manually identifies the rightmost and leftmost points to determine the total distance the motor needs to travel. Dividing this distance by 500 gives the number of images required in the X direction. This information is then entered into the GUI, which will be further explained in

the following section. Similarly, the same process is followed for the Y direction. The topmost and bottommost points of the smear are manually determined, and the number of images needed in the Y direction is calculated based on the total distance traveled by the motor divided by 500 steps. Similar steps are taken while using different objectives, but the step size determined between adjacent field of views should have an overlap of at least 10%.

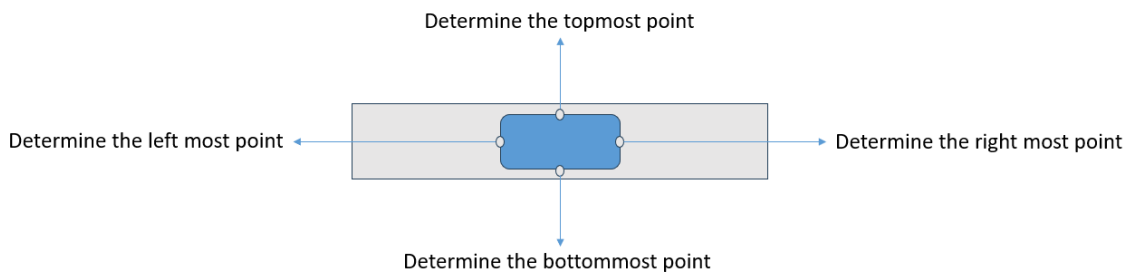


Figure 15 Manual inspection of the smear under the microscope to determine the four different points of the smear.

3.2.3.2 Capturing Image

To capture all the field of views in a whole slide image, the imaging process begins from the top right corner, then moves to the top left corner, and subsequently shifts one field of view downwards before moving to the right again. This pattern of movement forms an S shape across the sample stage to ensure comprehensive coverage of all fields of views. The resulting image is saved in RAW format, providing the raw sensor output that requires further processing to generate the final image. Figure 16 illustrates this process of capturing images in an S shape. Initially, we start with an initial estimate of focus at the first field of

view (FOV) and capture an image. Using this image, we estimate the focus for the adjacent FOV and move to that position, eliminating the need for separate autofocusing shots. We continue this process iteratively for subsequent FOVs, ensuring that adjacent areas are at nearly the same height to maintain focus consistency. This method minimizes the need for repeated acquisitions at the same spot and ensures continuous focus throughout the imaging

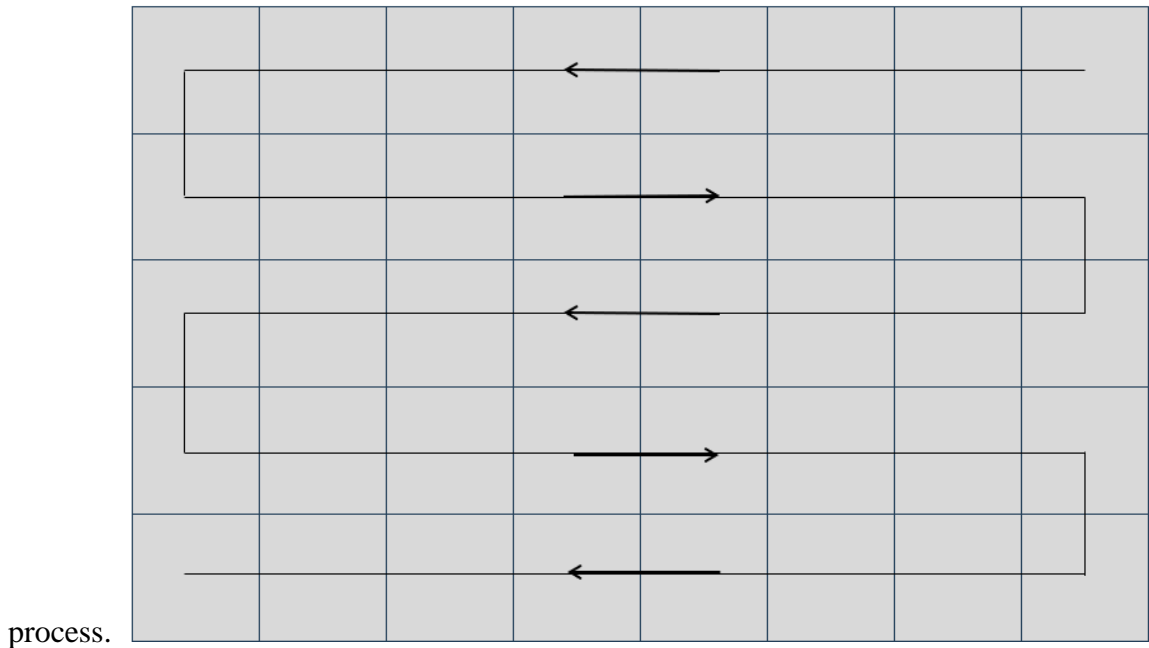


Figure 16 Stage translation in the X or Y direction moving in a S shaped pattern.

3.2.3.3 Image Stitching

ImageJ, a software utilized for Image Stitching, is an open-source image processing program specifically designed for scientific multidimensional images[36]. It stitches images together precisely in the same manner as they are captured for whole slide imaging. Within the ImageJ software, users have the flexibility to adjust the values for the X and Y grid, as well as modify the overlap between tiles. Additionally, there is an option called fusion method, which determines the manner in which the images are stitched together.

Various fusion techniques are available, including Linear Blending, Average, Median, Maximum Intensity, and Minimum Intensity. The choice of fusion technique depends on the type of images being captured. In Figure 17, a whole slide scan captured using the methods is depicted. For stitching this image, the overlap was set to 10%, and the X and Y grid size were both set to 15. The fusion method employed for this particular image was linear blending.



Figure 17 Stitched whole slide image using ImageJ software.

3.2.4 Graphical User Interface

To streamline the overall workflow, a Graphical User Interface (GUI) was developed using Python as the backend, utilizing the PyQt5 toolkit. The layout of the GUI is depicted in Figure 17, featuring multiple buttons and toggle buttons for various functionalities. Among the toggle buttons, one controls the LED, enabling users to toggle its state on and off. Another toggle button is provided to toggle the camera preview on and off. A text input field allows users to specify the file name, with a corresponding button to capture and save the image with the specified input. For motor control, there are six buttons in total facilitating movement in the positive and negative directions along the X, Y, and Z coordinates. Additionally, a button labelled "whole slide imaging" is available, allowing users to capture the entire smear region for later stitching using ImageJ. Lastly, a button labelled "Capture Stack" is provided, enabling the capture of a stack of data in the Z direction. This functionality was primarily utilized for capturing data for Autofocusing, as discussed in Chapter 2.

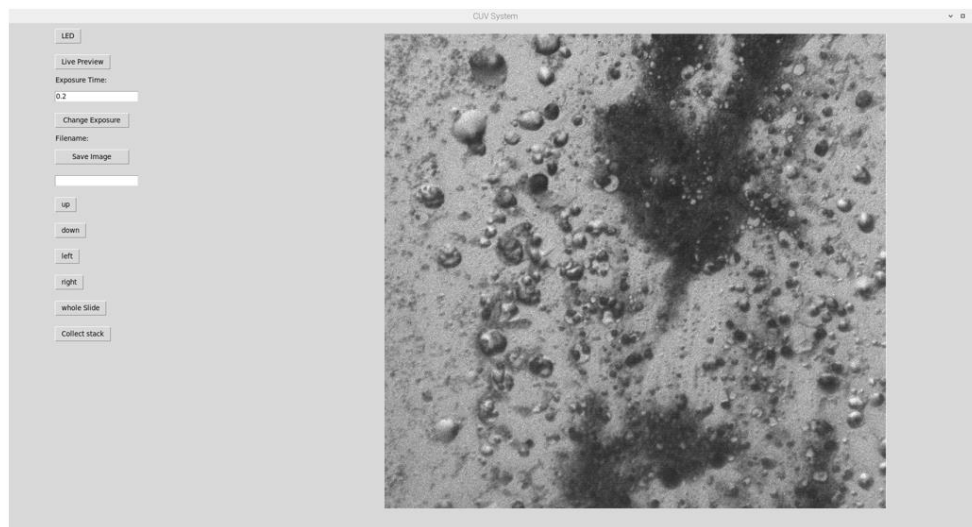


Figure 18 Graphical user interface Layout.

3.3 Discussion and Future Work

In this chapter, we delved into the technique employed for capturing whole slide imaging using the Compact UV System. Low-resolution stepper motors were utilized for the X and Y stages, while a high-resolution stepper motor was employed for the Z stage. Despite the overall functionality of the whole slide capturing technique being satisfactory, a few challenges were encountered during the process.

The first issue is that currently the Compact UV Microscopy requires approximately 15 minutes to scan and image a whole aspirate smear. This long scan time is due to hardware constraints (e.g., slow, precise stepper motors) and a relatively small field-of-view, requiring around 225 overlapping images per scan. This can be significantly improved with faster motors as high lateral translation accuracy is not critical for whole slide scanning applications and modified of system optics to provide a larger field-of-view, thus reducing the number of images required. The second challenge involved the autofocusing algorithm, which is based on a TensorFlow model. Due to the limited 4GB RAM capacity of the Raspberry Pi 4 model, deploying a deep learning model sometimes caused RAM issues. To address this in the future, the model could be deployed in a local desktop with a GPU, and raspberry pi can connect to this desktop while generating predictions enabling seamless predictions while data is being captured by the Compact UV System and alleviating the burden on the Raspberry Pi's RAM.

Furthermore, efforts should be made to reduce the time required for data capture to ideally one or two minutes. Additionally, deploying the image stitching algorithm directly on the

Raspberry Pi would streamline the process, allowing for all operations to be performed within the device itself.

CHAPTER 4. DEEP-ULTRAVIOLET MICROSCOPY FOR ANALYSIS OF BONE MARROW ASPIRATE ADEQUACY

4.1 Introduction

Bone marrow aspirates play a crucial role in diagnosing, staging, and monitoring hematologic conditions and cancers, such as leukemia, aplastic anemia, sickle cell disease, and solid tumor metastasis [37], [38]. Evaluating the adequacy of aspirates, as indicated by the presence of bony spicules, is crucial to ensure the procedural success and collection of relevant diagnostic material. Unfortunately, 8-50 percent of aspirations face challenges, including operator technique issues, hemodilution, or underlying pathologies, leading to unsuccessful outcomes [39]. The manual and error-prone nature of the process presents an opportunity to enhance patient outcomes through real-time and automated feedback on sample quality. More recently, some clinics have started having a bedside technician perform a naked eye inspection of unstained slides to help improve the success rate of bone marrow biopsies by identifying large spicules [40]. However, this technique is still not reliable for accurate, real-time feedback on aspirate adequacy.

Deep-ultraviolet (UV) microscopy enables label-free, high-resolution, quantitative molecular imaging by leveraging unique absorption properties of biomolecules, such as nucleic acids, in the UV region of the spectrum (200-400nm)[9], [9], [11], [12]. Recently, it has been demonstrated for fast hematology analysis of whole blood smears and blood samples in custom microfluidic cartridges for point-of-care applications enabled by advancements in low-cost UV LEDs and sensors [16], [17], [19], [31], [41]. UV microscopy has also been used for multi-spectral, label-free histopathology of tissue samples[20], [21], [42]. In these prior works, deep neural networks have been required to pseudo-colorize images to mimic conventional biochemical stains (i.e., hematoxylin and

eosin, Giemsa) [21], [31], [41]. In this study, we demonstrate a portable, LED-based UV microscope designed for rapid inspection of bone marrow aspirates, including real-time pseudo-colorization via a colormap transformation without any artificial intelligence (AI). We discuss results obtained from a clinical trial involving aspirate adequacy assessment from 51 pediatric patients showing excellent agreement between UV inspection of unstained slides and pathologist examination of stained slides. Furthermore, we demonstrate whole slide imaging with a previously developed low-cost UV system [31] and automated spicule detection via deep neural networks. Ultimately, we show that this device can be translated for bone marrow aspirate analysis in point-of-care applications.

4.2 Methods and Results

4.2.1 Portable, LED-based UV system

The UV microscope used in this system is similar to the system previously demonstrated for hematology analysis [31] but with minor modifications as shown in Fig. 19 below.

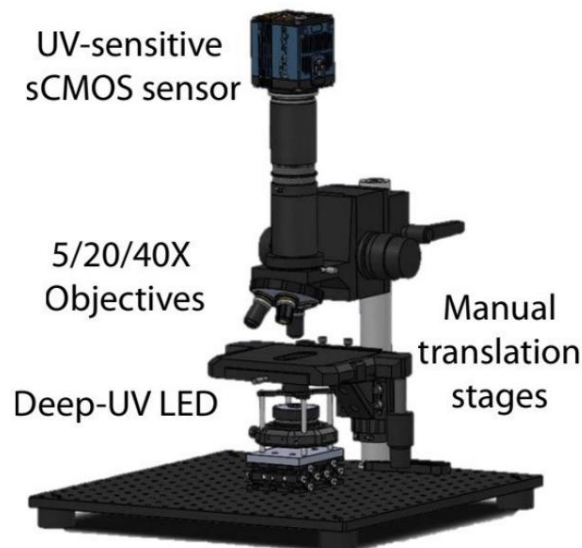


Figure 19 UV microscopy system for the assessment of bone marrow aspirate quality. [referred from [43]]

To accommodate UV-opaque glass microscope slides commonly used in the clinic for the preparation of bone marrow aspirate smears, a UV-bandpass filter, aligned with the 255nm LED used for illumination, was placed after the objective. This filter effectively screened out glass autofluorescence, permitting only the transmission of light at the illumination wavelength. To improve illumination power within the microscope's field of view (FOV) and mitigate glass absorption, a condenser lens module was introduced between the LED and the sample. Furthermore, the system incorporated manual translation stages to facilitate user-controlled slide translation and inspection. A turret housing 5/40X objective lenses was integrated to enable variable magnification during the inspection of bone marrow aspirate smears. This system was connected to a nearby PC for real-time visualization of samples in pseudocolored formats (Fig. 20), mimicking conventional May-Grunwald/Giemsa staining prior to hematopathologist inspection.

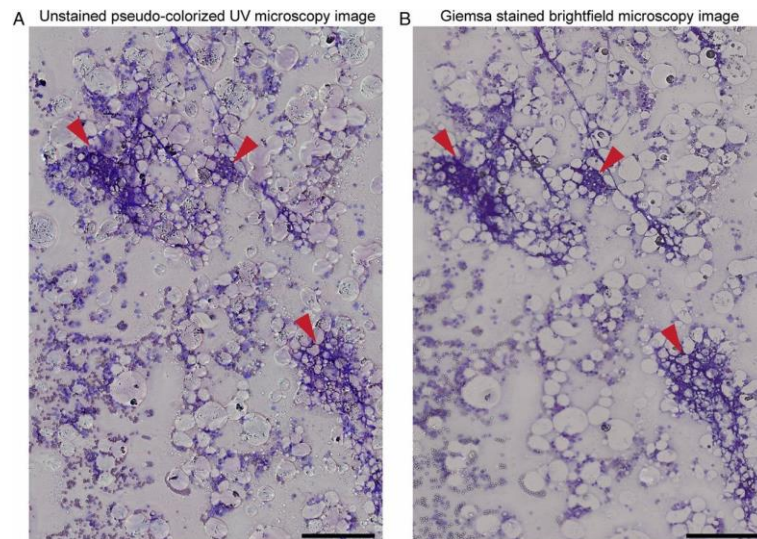


Figure 20 Wide-field unfixed and unstained pseudocolored UV image of a spiculated bone marrow aspirate (A) and the corresponding white-light bright-field microscopy image after fixing and staining (B). The red arrowheads point to spicules present in the smear [referenced from [16]].

4.2.2 Clinical Study

To validate the efficacy of the UV microscope system for real-time analysis of bone marrow aspirate adequacy, a clinical trial was conducted at the Aflac Sedation Suite at Children’s Healthcare of Atlanta, Egleston, involving 51 paediatric patients undergoing bone marrow aspiration. For each patient, a smear was prepared following the bone marrow aspiration procedure. This smear was first visually inspected by a bedside technician for the presence of spicules (naked eye examination). Then, the smear was immediately inspected on our UV microscope by a lab technician, who noted the presence or absence of spicules to determine if the aspiration was adequate. On average, this examination process was completed in less than two minutes. Subsequently, the sample was stained and inspected by a hematopathologist to check for the presence of spicules, establishing a reliable ground truth for comparison. The results from the clinical trial are summarized in Table 3 below.

Table 3 Results from the clinical study for bedside naked eye inspection (A) and visual UV inspection (B) of unstained bone marrow aspirate smears compared to ground truth histopathologist examination of stained slides. [referred from [44]]

(A) Bedside inspection results			(B) Visual UV inspection results		
	Pathologist +	Pathologist -		Pathologist +	Pathologist -
Bedside +	34	4	UV +	38	2
Bedside -	5	8	UV -	1	10

Accuracy	82.4%
Sensitivity	87.2%
Specificity	66.7%

Accuracy	94.1%
Sensitivity	97.4%
Specificity	83.3%

Results from the clinical trial comparing UV inspection of unstained slides with ground truth hematopathologist inspection of stained slides demonstrates high accuracy with our portable UV microscope system (94.1%). In comparison, the accuracy of the bedside inspection practice, becoming more widely adopted to improve clinical outcomes, was lower (82.3%). These results suggest that real-time feedback from our UV microscope offers an improvement in bone marrow aspirate adequacy assessment as compared to the current clinical gold standard, and thus could significantly reduce the number of bone marrow procedures performed.

4.2.3 Statistical Analysis

For the first clinical bone marrow aspirate smear for each patient, three blinded adequacy assessments were conducted. These included a bedside naked-eye inspection of the unstained slides, a deep UV inspection of the unstained slides, and an assessment by a pathologist of the stained slides. Accuracy, sensitivity, and specificity were calculated for the bedside and UV inspection assessments relative to the ground truth pathologist assessment across all 51 patients.

4.2.4 Deep Learning for Automated Spicule Detection

The YOLOv7 (You Only Look Once)[45], [46] is an object detection algorithm that was adapted to perform rapid object detection of bone marrow spicules in deep UV images. The dataset for this task included approximately 4300 images captured at 5X by the technicians from 51 smears during the clinical study (including 356 distinct spicules). The smear images were manually annotated for spicules and verified by hematopathologists.

Training and testing were conducted using a 5-fold cross-validation scheme. Specifically, 5 models were trained, each with training data comprising 80% of the acquired images, separated by patient ID. The remaining 20% of data was used for validation. During training, each full size (2048x2048p) image was cropped into 640x640p patches with approximately 10% overlap to be compatible with the chosen object detection network. The model's outputs on all patches were combined to generate a reconstructed image with the predicted bounding boxes. Then, non-maximum suppression was implemented to remove redundant bounding box predictions and improve the object detection accuracy. The network bounding box area thresholds were optimized via receiver operating characteristic (ROC) curve analysis and final detected spicule locations were extracted. This network was trained in Python 3.9 with PyTorch 1.11.0 on a NVIDIA GeForce RTX 2080Ti GPU for 100 epochs with a batch size of 8. An adequacy assessment was generated per patient ID and then compiled to compare with adequacy assessments from bedside assessment and visual UV inspection.

The developed workflow for automated spicule detection using the YOLOv7 object detection algorithm is shown in Figure 21 below. The field-of-view (FOV) of each input 5X image and cropped patches are 3.1x3.1mm and 0.96x0.96mm, respectively. During the algorithm implementation, model hyperparameters were optimized and each model's Mean Average Precision (MAP) was calculated, which is a common metric used for assessing object detection model performance. MAP can range from 0-69.7% with the YOLOv7 algorithm and the resulting average MAP of 66.9% indicates sufficient performance on par with other YOLOv7 implementations [45].

Output images from the test sets (Figure 22) clearly demonstrate accurate object detection in images with and w

without spicules. The resulting bounding boxes are generated in under 100ms per FOV and tightly surround detected spicule regions, distinctly highlighting their locations. Results from the automated deep UV inspection (Table 4) demonstrate an improvement in aspiration adequacy assessment compared to both the bedside inspection and visual deep UV inspection with an overall accuracy of 95.7% and sensitivity and specificity of 100% and 80.0%, respectively. We note the automated analysis only included data from 47 patients, as images were not collected for four patients by the technicians operating the UV microscope. The primary source of error during the automated adequacy assessment remained dense RBC clusters, which would be mitigated with larger datasets featuring more of these absorbing regions in the training data.[44]

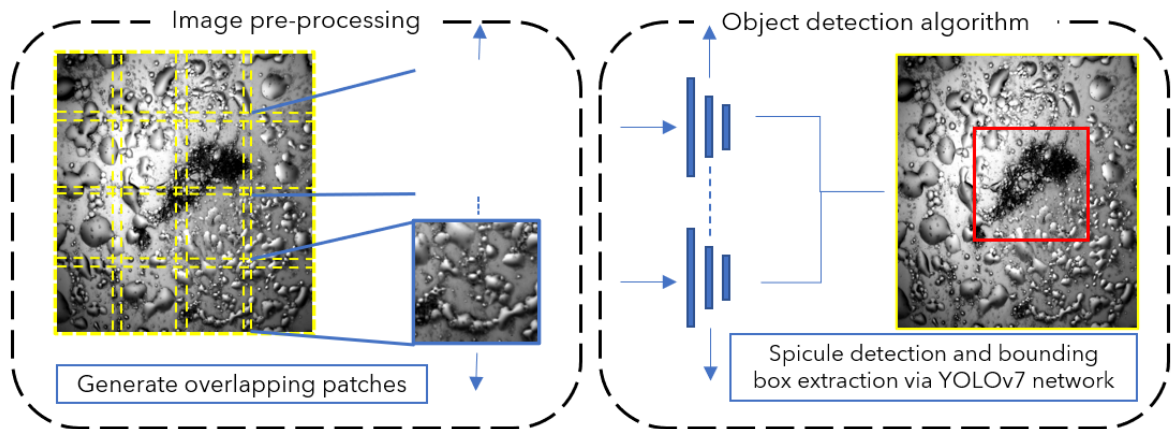


Figure 21 Automated spicule detection algorithm including UV image preprocessing and object detection steps[referred from [44]].

Table 4 Results from the clinical study for bedside naked eye inspection (A) and visual UV inspection (B) of unstained bone marrow aspirate smears compared to ground truth histopathologist examination of stained slides.[Referred from [44]]

Automated UV inspection results

	Pathologist +	Pathologist -
Bedside +	37	2
Bedside -	0	8

Accuracy	95.7%
Sensitivity	100%
Specificity	80.0%

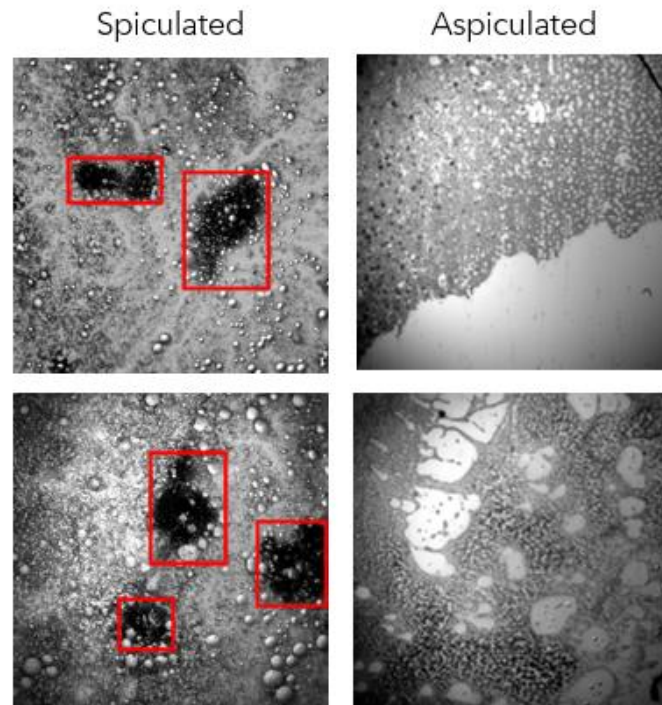


Figure 22 Sample network output images from images with (left) and without (right) spicules.[referred from [44]]

4.2.5 *Whole slide scanning via automated UV microscopy*

Select excess aspirate smears from the clinical study were imaged using a recently developed, low-cost deep UV microscope system[31]. This system is well-suited for point-of-care settings and enables automated whole slide scanning. Imaging was performed with 5X and 20X objective lenses corresponding with magnifications required to visualize spicules and individual cells, respectively. Each whole slide scan required ~225 images in a 15x15 grid with approximately 20% overlap. The resulting images were then stitched using an open-source algorithm (Grid collection/stitching plug-in, Fiji) which linearly blends overlapping image regions [24,25]. Following whole slide imaging with the compact deep UV system, each smear was fixed using methanol (ThermoFisher Scientific) for 15 minutes and stained in May Grünwald solution (MG500, Sigma Aldrich) for 10 minutes. After a brief rinse in phosphate buffered saline (PBS), the smear was stained with a 1:10 diluted Giemsa solution (GS500, Sigma Aldrich) for 20 minutes. Then, sample was washed in PBS again and air-dried prior to imaging. And imaged with a commercial color brightfield scanner (Cytation 7, Biotek) for comparison.

Paired deep UV whole slide scans of unstained smears and brightfield whole slide scans of stained smears were generated for several slides with varying levels of spicularity. Figure 20A includes whole slides scans at low magnification, demonstrating excellent concordance between pseudo-colored UV images and stained brightfield images. Spicules are distinguishable in these macro-scale scans (green dashed squares in Fig 23A), highlighting the potential for adequacy assessment from automated, low-magnification scans of unstained slides. Figure 23A (middle) also shows high magnification scans of smaller regions of interest containing spicules and diagnostically relevant marrow cells

including megakaryocytes (yellow arrows, right). Our simple pseudo-colorization algorithm mimics conventional staining even at smaller spatial scales. Corresponding images of an aspicular sample are also included (Fig. 23B) showing a lack of significant features at low and high magnification.[44]

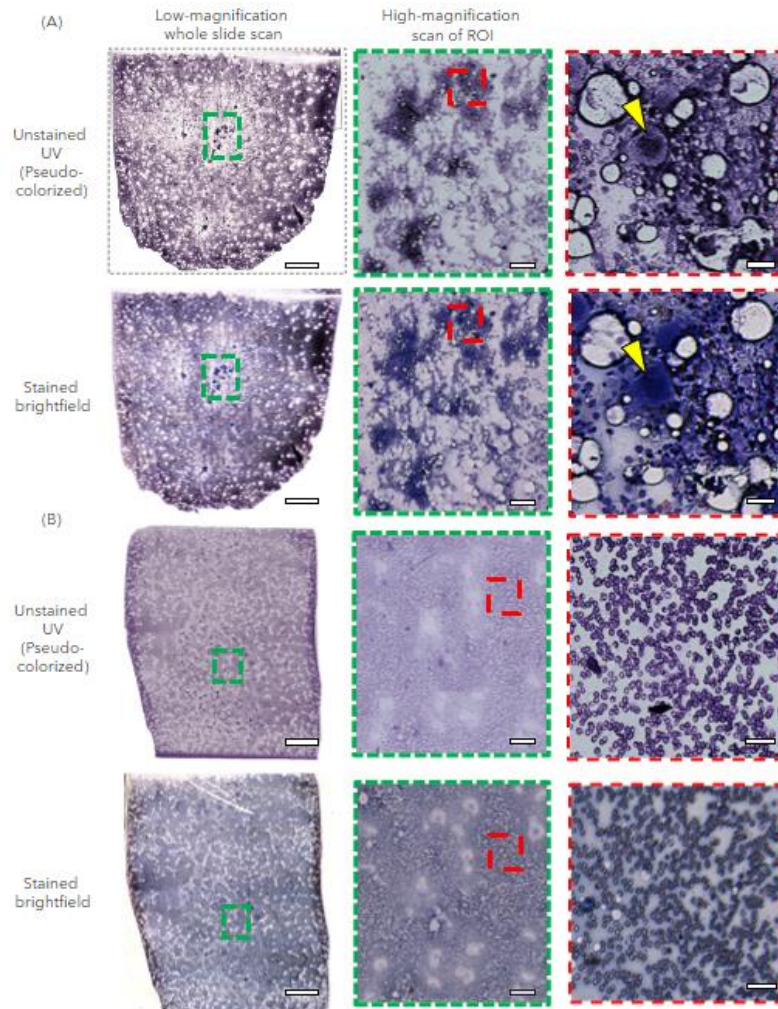


Figure 23 (A) Pseudo-colored UV whole slide scan of an unstained, spiculated bone marrow aspirate smear (top) and a brightfield whole slide scan of the same stained smear (bottom) captured at low (left) and high (middle, right) magnifications. (B) Corresponding whole slide scans for an aspicular bone marrow aspirate smear. Low and high magnification whole slide scans are composed of 225 images in a 15x15 grid with approximately 8% overlap. Yellow arrows indicate megakaryocytes present in the bone marrow aspirate. Scale bars: 3mm (left), 300µm (middle), and 40µm (right).[referred from [44]]

4.3 Discussion and Future Work

In this chapter, we introduce a portable UV microscope for real-time imaging of bone marrow aspirate smears, providing strong contrast in spicules and nucleated marrow cells. Our clinical study shows high accuracy in assessing adequacy through both visual and automated analysis of unstained smears compared to pathologist examination of stained slides. This improves current clinical practices, including bedside examinations of unstained smears. Additionally, we demonstrate automated whole-slide scanning with a low-cost UV microscope for easy visualization of smear morphology and spicule density.

This work presents the first automated and quantitative approach for assessment of bone marrow aspirate adequacy and has the potential to vastly improve the current standard of care. The technique presented in this work does not require biochemical stains or trained technicians, and thus can be broadly deployed for aspirate adequacy assessment at the point-of-care. In addition, the UV light used in this study does not damage samples over the time scales required for analysis and no alterations to smears were observed during the clinical study.

Limitations of the work presented here include misclassification of spicules by the developed automated analysis algorithm. This is likely due to the relatively small dataset size used for training our network and more training samples with distinct spicules would further improve classification accuracy. In addition, the adapted low-cost, automated UV microscope currently requires approximately 15 minutes to scan and image a whole aspirate smear. This long scan time is due to hardware constraints (e.g., slow, precise stepper motors) and a relatively small field-of-view, requiring around 225 overlapping

images per scan. This can be significantly improved with faster motors as high lateral translation accuracy is not critical for whole slide scanning applications and modified of system optics to provide a larger field-of-view, thus reducing the number of images required. Alternatively, a protocol capturing only a select random regions of a smear instead of an entire fill scan may also improve automated analysis speed without significantly affecting adequacy assessment accuracy.

CHAPTER 5. CONCLUSION

In this study, we embarked on a journey to expand the capabilities of UV microscopy by leveraging existing simple, low-cost systems and custom benchtop multispectral microscopes, with a focus on enhancing point-of-care applications through the integration of Artificial Intelligence (AI) techniques. The comprehensive aims of this project were:

1. **Implementation of Single-Shot Autofocusing in UV Microscopy:** We successfully implemented a single-shot autofocusing mechanism in UV microscopy, enabling rapid and efficient adjustment of focus without the need for time-consuming manual adjustments. This advancement streamlines the imaging process and enhances overall efficiency, laying the foundation for improved point-of-care diagnostics and research applications.
2. **Development of an Algorithm for Automating Spicule Detection:** Through rigorous algorithm development and testing, we have achieved significant progress in automating the detection of spicules in UV microscopy images. By leveraging AI techniques, we have demonstrated the feasibility of accurately identifying and analyzing spicule structures, facilitating enhanced diagnostic capabilities.
3. **Implementation of a Strategy for Whole Slide Imaging Using Deep UV Microscopy:** Building upon existing methodologies, we have devised a robust strategy for capturing whole slide images of samples using deep UV microscopy.

The achievements made in this study hold significant implications for the field of UV microscopy, particularly in the realms of healthcare and research. By enhancing the efficiency, accuracy, and applicability of UV microscopy techniques, our work contributes

to the advancement of diagnostic capabilities, disease understanding, and biomedical research.

Looking ahead, several avenues for future research emerge. Further refinement and optimization of AI algorithms for spicule detection could lead to even greater accuracy and efficiency in identifying subtle morphological features. Additionally, exploring lighter models for autofocusing could help in deploying the algorithm in a very affordable microcontroller.

In conclusion, this study represents a significant step forward in the advancement of UV microscopy techniques. By successfully implementing single-shot autofocusing, automating spicule detection, and devising a strategy for whole slide imaging, we have demonstrated the potential of UV microscopy to revolutionize point-of-care diagnostics and biomedical research. As we continue to explore and innovate in this field, the possibilities for further enhancing the capabilities of UV microscopy are vast, promising continued progress and innovation in the years to come.

REFERENCES

- [1] H. S. Liu, M. S. Jan, C. K. Chou, P. H. Chen, and N. J. Ke, “Is green fluorescent protein toxic to the living cells?,” *Biochem. Biophys. Res. Commun.*, vol. 260, no. 3, pp. 712–717, Jul. 1999, doi: 10.1006/bbrc.1999.0954.
- [2] U. Neugebauer, J. H. Clement, T. Bocklitz, C. Krafft, and J. Popp, “Identification and differentiation of single cells from peripheral blood by Raman spectroscopic imaging,” *J. Biophotonics*, vol. 3, no. 8–9, pp. 579–587, Aug. 2010, doi: 10.1002/jbio.201000020.
- [3] A. Ramoji *et al.*, “Toward a Spectroscopic Hemogram: Raman Spectroscopic Differentiation of the Two Most Abundant Leukocytes from Peripheral Blood,” *Anal. Chem.*, vol. 84, no. 12, pp. 5335–5342, Jun. 2012, doi: 10.1021/ac3007363.
- [4] B. P. Yakimov *et al.*, “Label-free characterization of white blood cells using fluorescence lifetime imaging and flow-cytometry: molecular heterogeneity and erythrophagocytosis [Invited],” *Biomed. Opt. Express*, vol. 10, no. 8, pp. 4220–4236, Aug. 2019, doi: 10.1364/BOE.10.004220.
- [5] T. Horio and H. Hotani, “Visualization of the dynamic instability of individual microtubules by dark-field microscopy,” *Nature*, vol. 321, no. 6070, pp. 605–607, Jun. 1986, doi: 10.1038/321605a0.
- [6] G. S. Verebes, M. Melchiorre, A. Garcia-Leis, C. Ferreri, C. Marzetti, and A. Torreggiani, “Hyperspectral enhanced dark field microscopy for imaging blood cells,” *J. Biophotonics*, vol. 6, no. 11–12, pp. 960–967, 2013, doi: 10.1002/jbio.201300067.
- [7] K. Lee *et al.*, “Quantitative Phase Imaging Techniques for the Study of Cell Pathophysiology: From Principles to Applications,” *Sensors*, vol. 13, no. 4, Art. no. 4, Apr. 2013, doi: 10.3390/s130404170.
- [8] Y. Park, C. Depeursinge, and G. Popescu, “Quantitative phase imaging in biomedicine,” *Nat. Photonics*, vol. 12, no. 10, pp. 578–589, Oct. 2018, doi: 10.1038/s41566-018-0253-x.
- [9] S. Soltani, A. Ojaghi, and F. E. Robles, “Deep UV dispersion and absorption spectroscopy of biomolecules,” *Biomed. Opt. Express*, vol. 10, no. 2, pp. 487–499, Feb. 2019, doi: 10.1364/BOE.10.000487.
- [10] B. J. Zeskind, “Quantitative imaging of living cells by deep ultraviolet microscopy,” Thesis, Massachusetts Institute of Technology, 2006. Accessed: Apr. 22, 2024. [Online]. Available: <https://dspace.mit.edu/handle/1721.1/38693>

- [11] B. J. Zeskind *et al.*, “Nucleic acid and protein mass mapping by live-cell deep-ultraviolet microscopy,” *Nat. Methods*, vol. 4, no. 7, pp. 567–569, Jul. 2007, doi: 10.1038/nmeth1053.
- [12] M. C. Cheung, J. G. Evans, B. McKenna, and D. J. Ehrlich, “Deep Ultraviolet Mapping of Intracellular Protein and Nucleic Acid in Femtograms per Pixel,” *Cytom. Part J. Int. Soc. Anal. Cytol.*, vol. 79, no. 11, pp. 920–932, Nov. 2011, doi: 10.1002/cyto.a.21111.
- [13] M. C. Cheung, R. LaCroix, B. K. McKenna, L. Liu, J. Winkelman, and D. J. Ehrlich, “Intracellular protein and nucleic acid measured in eight cell types using deep-ultraviolet mass mapping,” *Cytom. Part J. Int. Soc. Anal. Cytol.*, vol. 83, no. 6, pp. 540–551, Jun. 2013, doi: 10.1002/cyto.a.22277.
- [14] A. Ojaghi, M. E. Fay, W. A. Lam, and F. E. Robles, “Ultraviolet Hyperspectral Interferometric Microscopy,” *Sci. Rep.*, vol. 8, no. 1, p. 9913, Jul. 2018, doi: 10.1038/s41598-018-28208-0.
- [15] N. Kaza, A. Ojaghi, and F. E. Robles, “Ultraviolet hyperspectral microscopy using chromatic-aberration-based iterative phase recovery,” *Opt. Lett.*, vol. 45, no. 10, pp. 2708–2711, May 2020, doi: 10.1364/OL.392634.
- [16] A. Ojaghi *et al.*, “Label-free hematology analysis using deep-ultraviolet microscopy,” *Proc. Natl. Acad. Sci.*, vol. 117, no. 26, pp. 14779–14789, Jun. 2020, doi: 10.1073/pnas.2001404117.
- [17] N. Kaza, A. Ojaghi, and F. E. Robles, “Hemoglobin quantification in red blood cells via dry mass mapping based on UV absorption,” *J. Biomed. Opt.*, vol. 26, no. 8, p. 086501, Aug. 2021, doi: 10.1117/1.JBO.26.8.086501.
- [18] A. Ojaghi, P. Casteleiro Costa, C. Caruso, W. A. Lam, and F. E. Robles, “Label-free automated neutropenia detection and grading using deep-ultraviolet microscopy,” *Biomed. Opt. Express*, vol. 12, no. 10, pp. 6115–6128, Sep. 2021, doi: 10.1364/BOE.434465.
- [19] A. Ojaghi *et al.*, “Label-free deep-UV microscopy detection and grading of neutropenia using a passive microfluidic device,” *Opt. Lett.*, vol. 47, no. 22, pp. 6005–6008, Nov. 2022, doi: 10.1364/OL.472691.
- [20] S. Soltani, B. Cheng, A. O. Osunkoya, and F. E. Robles, “Deep UV Microscopy Identifies Prostatic Basal Cells: An Important Biomarker for Prostate Cancer Diagnostics,” *BME Front.*, vol. 2022, p. 9847962, Oct. 2022, doi: 10.34133/2022/9847962.
- [21] S. Soltani *et al.*, “Prostate cancer histopathology using label-free multispectral deep-UV microscopy quantifies phenotypes of tumor aggressiveness and enables multiple diagnostic virtual stains,” *Sci. Rep.*, vol. 12, no. 1, p. 9329, Jun. 2022, doi: 10.1038/s41598-022-13332-9.

- [22] B. S. Veeling, J. Linmans, J. Winkens, T. Cohen, and M. Welling, "Rotation Equivariant CNNs for Digital Pathology." arXiv, Jun. 08, 2018. Accessed: Apr. 22, 2024. [Online]. Available: <http://arxiv.org/abs/1806.03962>
- [23] S. Sharma, S. Kumar, M. Sharma, and A. Kalkal, "An ensemble of deep CNNs for automatic grading of breast cancer in digital pathology images," *Neural Comput. Appl.*, vol. 36, no. 11, pp. 5673–5693, Apr. 2024, doi: 10.1007/s00521-023-09368-1.
- [24] C. C. Atabansi, J. Nie, H. Liu, Q. Song, L. Yan, and X. Zhou, "A survey of Transformer applications for histopathological image analysis: New developments and future directions," *Biomed. Eng. OnLine*, vol. 22, no. 1, p. 96, Sep. 2023, doi: 10.1186/s12938-023-01157-0.
- [25] Y. Luo, L. Huang, Y. Rivenson, and A. Ozcan, "Single-Shot Autofocusing of Microscopy Images Using Deep Learning," *ACS Photonics*, vol. 8, no. 2, pp. 625–638, Feb. 2021, doi: 10.1021/acsp Photonics.0c01774.
- [26] L. Jose, S. Liu, C. Russo, A. Nadort, and A. Di Ieva, "Generative Adversarial Networks in Digital Pathology and Histopathological Image Processing: A Review," *J. Pathol. Inform.*, vol. 12, p. 43, Nov. 2021, doi: 10.4103/jpi.jpi_103_20.
- [27] J. F. Brenner, B. S. Dew, J. B. Horton, T. King, P. W. Neurath, and W. D. Selles, "An automated microscope for cytologic research a preliminary evaluation.," *J. Histochem. Cytochem.*, vol. 24, no. 1, pp. 100–111, Jan. 1976, doi: 10.1177/24.1.1254907.
- [28] S. Bengesi, H. El-Sayed, K. Sarker, Y. Houkpati, and T. Oladunni, "Advancements in Generative AI: A Comprehensive Review of GANs, GPT, Autoencoders, Diffusion Model, and Transformers."
- [29] L. Alzubaidi *et al.*, "Review of deep learning: concepts, CNN architectures, challenges, applications, future directions," *J. Big Data*, vol. 8, no. 1, p. 53, Mar. 2021, doi: 10.1186/s40537-021-00444-8.
- [30] A. Dash, J. Ye, and G. Wang, "A review of Generative Adversarial Networks (GANs) and its applications in a wide variety of disciplines -- From Medical to Remote Sensing." arXiv, Oct. 01, 2021. Accessed: Apr. 23, 2024. [Online]. Available: <http://arxiv.org/abs/2110.01442>
- [31] V. Gorti, N. Kaza, E. K. Williams, W. A. Lam, and F. E. Robles, "Compact and low-cost deep-ultraviolet microscope system for label-free molecular imaging and point-of-care hematological analysis," *Biomed. Opt. Express*, vol. 14, no. 3, pp. 1245–1255, Mar. 2023, doi: 10.1364/BOE.482294.
- [32] M. Sandler, A. Howard, M. Zhu, A. Zhmoginov, and L.-C. Chen, "MobileNetV2: Inverted Residuals and Linear Bottlenecks." arXiv, Mar. 21, 2019. Accessed: Apr. 22, 2024. [Online]. Available: <http://arxiv.org/abs/1801.04381>

- [33] “What is MobileNetV2? Features, Architecture, Application and More.” Accessed: Apr. 22, 2024. [Online]. Available: <https://www.analyticsvidhya.com/blog/2023/12/what-is-mobilenetv2/>
- [34] F. Ghaznavi, A. Evans, A. Madabhushi, and M. Feldman, “Digital Imaging in Pathology: Whole-Slide Imaging and Beyond,” *Annu. Rev. Pathol. Mech. Dis.*, vol. 8, no. Volume 8, 2013, pp. 331–359, Jan. 2013, doi: 10.1146/annurev-pathol-011811-120902.
- [35] Z. Bian *et al.*, “Autofocusing technologies for whole slide imaging and automated microscopy,” *J. Biophotonics*, vol. 13, no. 12, p. e202000227, 2020, doi: 10.1002/jbio.202000227.
- [36] J. Schindelin *et al.*, “Fiji: an open-source platform for biological-image analysis,” *Nat. Methods*, vol. 9, no. 7, pp. 676–682, Jun. 2012, doi: 10.1038/nmeth.2019.
- [37] B. J. Bain, “Bone marrow aspiration,” *J. Clin. Pathol.*, vol. 54, no. 9, pp. 657–663, Sep. 2001, doi: 10.1136/jcp.54.9.657.
- [38] Malempati Suman, Joshi Sarita, Lai Susanna, Braner Dana A.V., and Tegtmeyer Ken, “Bone Marrow Aspiration and Biopsy,” *N. Engl. J. Med.*, vol. 361, no. 15, p. e28, 2009, doi: 10.1056/NEJMvcm0804634.
- [39] J. A. Hawing, O. G. Cantu Rodriguez, A. Gómez-De León, C. Mancias, L. del C. Tarín Arzaga, and D. Gomez-Almaguer, “Aspicular Bone Marrow Aspiration: A Common, but Not a Minor Problem,” *Blood*, vol. 134, no. Supplement_1, p. 5841, Nov. 2019, doi: 10.1182/blood-2019-131662.
- [40] O. O. Odejide *et al.*, “Improving the quality of bone marrow assessment: Impact of operator techniques and use of a specimen preparation checklist,” *Cancer*, vol. 119, no. 19, pp. 3472–3478, Oct. 2013, doi: 10.1002/cncr.28249.
- [41] N. Kaza, A. Ojaghi, and F. E. Robles, “Virtual Staining, Segmentation, and Classification of Blood Smears for Label-Free Hematology Analysis,” *BME Front.*, vol. 2022, p. 9853606, Jul. 2022, doi: 10.34133/2022/9853606.
- [42] S. Ye *et al.*, “Rapid and label-free histological imaging of unprocessed surgical tissues via dark-field reflectance ultraviolet microscopy,” *iScience*, vol. 26, no. 1, p. 105849, Dec. 2022, doi: 10.1016/j.isci.2022.105849.
- [43] V. Gorti, A. R. Subramanian, A. Aljudi, W. Aumann, and F. Robles, “Deep-ultraviolet microscopy for analysis of bone marrow aspirate adequacy,” in *Optical Diagnostics and Sensing XXIV: Toward Point-of-Care Diagnostics*, SPIE, Mar. 2024, pp. 121–125. doi: 10.1117/12.3002646.
- [44] V. Gorti *et al.*, “Rapid, point-of-care bone marrow aspirate adequacy assessment via deep ultraviolet microscopy”. (In preparation)

- [45] C.-Y. Wang, A. Bochkovskiy, and H.-Y. M. Liao, “YOLOv7: Trainable bag-of-freebies sets new state-of-the-art for real-time object detectors.” arXiv, Jul. 06, 2022. Accessed: Apr. 22, 2024. [Online]. Available: <http://arxiv.org/abs/2207.02696>
- [46] M. Rahaman, *The Current Trends of Object Detection Algorithms: A Review*. 2023. doi: 10.13140/RG.2.2.19067.49442.